e-ISSN: 2805-5756

PENERBIT PRESS
UNIVERSITI TEKNOLOGI MARA

Available online at
https://jaeds.uitm.edu.my

Journal of Applied Engineering Design and Simulation 6(2) 2026, 27-47

Journal of Applied Engineering Design and Simulation

Actuator-level kinematic analysis of a PAM-driven dual four-bar knee exoskeleton for rehabilitation gait assistance

F. Jani[1], T. M. A. T. Asmadi[2], M. H. M. Ramli[3]*, W. S. W. Mohamad[3]

[1]*Institute of Postgraduate Studies, Faculty of Mechanical Engineering, Universiti Teknologi MARA, Shah Alam, 40450 Selangor, Malaysia.*
[2]*Faculty of Mechanical Engineering, Universiti Teknologi MARA, 40450 Shah Alam, Selangor, Malaysia.*
[3]*Department of Control and Engineering, Faculty of Mechanical Engineering, Universiti Teknologi MARA, Shah Alam 40450 Selangor, Malaysia*

ARTICLE INFO

Article history:
Received 05 June 2026
Revised 13 August 2026
Accepted 19 August 2026
Online first 25 September 2026
Published 25 September 2026

Keywords:
Knee exoskeleton
Dual four-bar linkage
Pneumatic artificial muscle
Gait rehabilitation
Closed-loop kinematics

DOI:

10.24191/jaeds.v6i2.199

ABSTRACT

Stroke-related gait impairment commonly produces reduced knee coordination and insufficient toe clearance, motivating the development of compliant rehabilitation exoskeletons. Pneumatic artificial muscles (PAMs) offer compliant, biomimetic actuation well suited to rehabilitation gait training; however, existing four-bar linkage exoskeleton studies have focused on mechanism synthesis and joint-level trajectory reproduction without analytically characterising the continuous actuator-level kinematic demands that PAM actuation imposes across the gait cycle. This study develops a closed-loop kinematic framework for a PAM-driven dual four-bar knee exoskeleton, actuated by Festo DMSP-20 fluidic muscles, that maps prescribed rehabilitation knee trajectories to actuator displacement and contraction-rate demands at the preliminary design stage. The mechanism was reconstructed from the KNEXO structural concept using MotionGen simulation and modelled analytically through vector loop-closure analysis and Freudenstein's equation. A continuous quartic stroke-map formulation was introduced to replace repeated inverse-kinematic computation with a single analytical expression, enabling efficient actuator evaluation throughout the gait cycle. The reconstructed mechanism reproduced the normative knee trajectory with a root-mean-square error of 2.69° over the eight gait-event boundaries, with all gait-event angles remaining within the Perry normative variability band and Freudenstein loop-closure residuals below 5% for both the primary and secondary mechanisms. All PAM contractions remained below 20% of the nominal actuator length, within the 25% practical operating limit of the selected actuator, while the quartic stroke-map reproduced the

[3*]Corresponding author. *E-mail address*: haniframli@uitm.edu.my

actuator-contraction relationship with root-mean-square errors of 0.23 cm and 0.37 cm. The proposed framework provides designers with an analytical tool for evaluating actuator contraction displacement, contraction-rate demands, and transmission kinematics in dual four-bar rehabilitation exoskeletons before committing to hardware fabrication.

Nomenclature

a, b, c, d	input, coupler, output, and ground link lengths of a four-bar mechanism (mm)
K_1, K_2, K_3	Freudenstein constants
l_f, l_t, l_{ft}	femur, tibia, and foot segment lengths (m)
l_i	length of link i (mm)
L_i	instantaneous pneumatic actuator length (cm)
L_0	nominal (rest) actuator length (cm)
p_k, p_a, p_t	knee, ankle and toe position vectors (m)
Δ_i	pneumatic actuator contraction of mechanism i (cm)
$\dot{\Delta}_i$	actuator contraction rate (cm/s)
$\theta_h, \theta_k, \theta_a$	hip, knee and ankle flexion–extension angles (°)
θ_i	absolute orientation angle of link i (°)
θ_2, θ_4	four-bar input and output angles (°)
$\dot{\theta}$	knee angular velocity (rad/s)

Abbreviations

HS	heel strike (initial contact)
ISW	initial swing
LR	loading response
LSPB	linear segment with parabolic blends
MS	mid-stance
MSW	mid-swing
PAM	pneumatic artificial muscle
PS	pre-swing
ROM	range of motion
TS	terminal stance
TSW	terminal swing

1. INTRODUCTION

Stroke is the second leading cause of death and the third leading cause of disability worldwide, with approximately 12 million new cases each year [1]. Among survivors, reduced knee flexion–extension coordination and diminished toe clearance are persistent gait deficits that compromise safe, independent walking [2]. Powered lower-limb exoskeletons have emerged as a rehabilitation tool for restoring coordinated gait through repetitive, physiologically consistent joint-trajectory guidance [3].

Most lower-limb exoskeletons use electric motors for their precise position control [4], but such systems exhibit rigid mechanical behaviour and limited compliance during physical human–robot

interaction, which can compromise comfort and safety during involuntary or spastic patient movements [5]. PAMs offer an alternative with inherent compliance, a high power-to-weight ratio, and biomimetic contraction behaviour [6]. Beyl et al. [5], [7] demonstrated this in the KNEXO exoskeleton, where pleated PAMs provided safe, adaptable gait assistance during treadmill walking, and compliant actuation has since become recognised as a fundamental requirement for safe gait training [8]. PAMs, however, produce linear contraction rather than rotational torque, and therefore require a transmission mechanism to convert actuator displacement into knee rotation.

The transmission choice is equally important. Many exoskeletons adopt a single-axis revolute knee joint for simplicity, but this cannot reproduce the polycentric motion of the biological knee [9] and may introduce kinematic misalignment and discomfort [10]. Four-bar linkages are a widely adopted alternative, approximating natural knee kinematics within a compact planar configuration [9], [11]. They are particularly suited to PAM-driven systems because they form a closed-loop transmission that geometrically couples linear actuator contraction to rotational knee motion, enabling analytical characterisation of the actuator–joint relationship.

Recent four-bar exoskeleton designs have focused on mechanism synthesis and optimisation [9], [11], with Kittisares et al. [10] extending the concept to a dual four-bar configuration with hydraulic artificial muscles. None of these studies, however, extends the analysis to the continuous actuator-level kinematic behaviour imposed across a complete gait cycle: the actuator displacement and contraction-rate demands that the chosen trajectory imposes on the muscle remain uncharacterised. For a PAM-driven dual four-bar system, this actuator-level characterisation is what allows a designer to verify, before fabrication, that the required contractions remain within the practical operating range and that the transmission produces feasible actuator demands across all gait phases. Specifically, Kittisares et al. [10] optimised the dual four-bar geometry with a genetic algorithm to minimise human–exoskeleton knee misalignment and validated stair-ascent assistance experimentally, but did not characterise the continuous actuator-level displacement and contraction-rate demands imposed by a prescribed joint trajectory, nor establish a continuous analytical actuator–joint relationship — the actuator-level characterisation that the present framework provides.

This paper develops an analytical kinematic framework for a PAM-driven dual four-bar knee exoskeleton that predicts actuator-level kinematic demands at the preliminary design stage. The KNEXO structural concept [5] is reconstructed using MotionGen [12] and modelled analytically through vector loop-closure analysis and Freudenstein's equation, establishing the closed-loop relationship between knee rotation and PAM contraction. A continuous analytical quartic stroke-map is then introduced to evaluate actuator displacement and contraction rate throughout the gait cycle without repeated inverse-kinematic computation. The main contributions of this paper are:

1. A closed-loop kinematic framework that analytically maps prescribed rehabilitation knee trajectories to PAM actuator displacement and contraction-rate demands through a dual four-bar linkage, enabling actuator-feasibility assessment prior to hardware fabrication.
2. An analytical quartic stroke-map formulation that provides continuous actuator evaluation without repeated inverse-kinematic computation, offering a computationally efficient tool for preliminary actuator contraction evaluation and trajectory planning.

The remainder of this paper is organised as follows. Section 2 presents the reference gait modelling, the human lower-limb kinematic simulation, and the design and analytical kinematic formulation of the

proposed exoskeleton. Section 3 presents the gait-model validation, mechanism verification, actuator stroke evaluation, and velocity kinematic analysis. Section 4 concludes the paper and outlines future work.

2. REFERENCE GAIT MODELLING AND EXOSKELETON KINEMATIC DESIGN FRAMEWORK

This section derives the actuator-level kinematic requirements from physiological gait data. A sagittal-plane knee trajectory is first established as a biomechanical baseline in Section 2.1 and reproduced by a simplified lower-limb model in Section 2.2. It is then mapped to actuator displacement and contraction-rate demands through closed-loop analysis of the proposed dual four-bar PAM-driven exoskeleton in Section 2.3.

2.1 Reference gait patterns and requirements

Normal human gait is adopted as the biomechanical reference for defining the knee-motion targets of the proposed exoskeleton. Although post-stroke gait deviates from normal patterns through reduced speed, altered phase timing and decreased toe clearance [2], normal gait remains a stable, clinically validated baseline. It is widely used as the therapeutic target in robotic gait training to promote motor relearning, gait symmetry and functional recovery [3].

A complete gait cycle comprises two periods — stance (heel strike to toe-off) and swing (toe-off to the next heel strike). Following Perry and Burnfield [13], the cycle is divided into eight standard phases: heel strike / initial contact (HS), loading response (LR), mid-stance (MS), terminal stance (TS), pre-swing (PS), initial swing (ISW), mid-swing (MSW) and terminal swing (TSW), as illustrated in Figure 1. Toe-off — the instant the foot leaves the ground, and stance gives way to swing — occurs at the pre-swing/initial-swing boundary, at approximately 60% of the gait cycle.

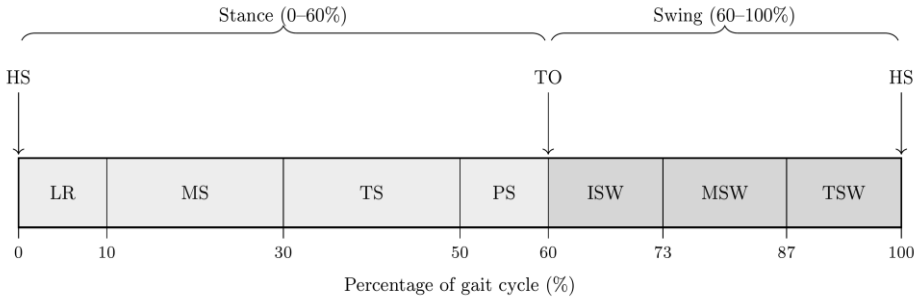


Fig. 1. Normal human gait cycle showing the eight standard phases and their percentage boundaries; toe-off marks the stance-to-swing transition at approximately 60% of the cycle

The gait-cycle duration is fixed at 2 s, within the slow-walking range reported for post-stroke hemiparetic gait and consistent with the reduced speeds adopted in rehabilitation exoskeletons for safety and motor relearning [5], [14]. The phase boundaries are converted from percentage intervals to absolute time in Table 1 to synchronise them with the time-dependent joint trajectories used in the subsequent actuator analysis.

Table 1. Gait-phase transitions with the corresponding percentage of the gait cycle and absolute time intervals for the 2 s cycle

Gait Phase	% Gait Cycle	Time Interval (s)
HS – LR	0 – 10	0 – 0.20
LR – MS	10 – 30	0.20 – 0.60
MS – TS	30 – 50	0.60 – 1.00
TS – PS	50 – 60	1.00 – 1.20
PS – ISW	60 – 73	1.20 – 1.46
ISW – MSW	73 – 87	1.46 – 1.74
MSW – TSW	87 – 100	1.74 – 2.00

Source: Adapted from Perry and Burnfield [13]; time intervals calculated by the authors

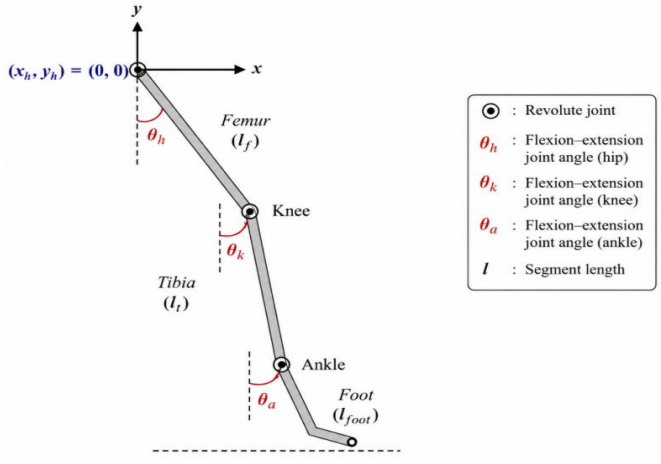


Fig. 2. Sagittal-plane three-segment model of the human lower limb (femur, tibia and foot) with revolute joints at the hip, knee and ankle

2.2 Human lower-limb gait model

A simplified sagittal-plane kinematic model of the human lower limb generates the reference knee trajectory and toe-clearance profile used in the exoskeleton transmission analysis. The limb is represented as three rigid segments — femur, tibia and foot — connected by revolute joints at the hip, knee and ankle in Figure 2. Motion is confined to the sagittal plane; soft-tissue deformation, structural compliance and out-of-plane motion are neglected, and the hip is fixed proximally to isolate the kinematic contribution of the lower-limb segments. Ground reaction forces and foot–ground contact are not modelled, consistent with the kinematic scope of the analysis. This three-segment representation is widely used in rehabilitation exoskeleton design and captures the joint motion that dominates level walking [13], [15].

The configuration is described by the flexion–extension rotations at the hip, knee and ankle (θh, θk, and θa), each measured from the downward vertical with positive rotation corresponding to forward flexion. A global frame is fixed at the hip, with x directed forward and y upward. Segment lengths are assigned from Winter's anthropometric proportions for a 1.75 m reference body height [15], giving femur, tibia and foot lengths of 0.429 m, 0.431 m and 0.266 m respectively.

Because the joint angles act cumulatively along the kinematic chain, the absolute orientation of each segment is the sum of the preceding joint rotations. The knee, ankle and toe positions are obtained by propagation from the hip origin:

$$p_k = \begin{bmatrix} l_f \sin\theta_h \\ -l_f \cos\theta_h \end{bmatrix} \quad \text{(m)} \quad (1)$$

$$p_a = p_k + \begin{bmatrix} l_t \sin(\theta_h + \theta_k) \\ -l_t \cos(\theta_h + \theta_k) \end{bmatrix} \quad \text{(m)} \quad (2)$$

$$p_t = p_a + \begin{bmatrix} l_{ft} \sin(\theta_h + \theta_k + \theta_a) \\ -l_{ft} \cos(\theta_h + \theta_k + \theta_a) \end{bmatrix} \quad \text{(m)} \quad (3)$$

where l_f, l_t and l_{ft} are the femur, tibia and foot lengths defined above. The toe vector is treated as a kinematic reference point for vertical limb-end excursion during swing rather than the exact anatomical toe position, which is sufficient for assessing periodic swing-phase clearance [13], [15].

The model was implemented in GNU Octave 11.1.0 (GNU Project, free software under GPLv3). Normative sagittal-plane joint-angle trajectories for the hip, knee and ankle were prescribed as time-dependent inputs over the 2 s gait cycle defined in Section 2.1, and the knee, ankle and toe positions were evaluated from Eq. (1)–(3). The joint range of motion (ROM) was taken as the difference between the maximum and minimum joint angle within the cycle, and the vertical toe clearance as the maximum toe elevation above its lowest stance-phase position. The resulting joint trajectories, ROM and toe-clearance profile are validated against normative benchmarks in Section 3.1 and then used as the biomechanical reference for the exoskeleton kinematic modelling in Section 2.3.

2.3 Design and kinematic modelling of the lower-limb exoskeleton

Building on the validated lower-limb model of Section 2.2, this section presents the design of the proposed dual four-bar knee exoskeleton driven by pneumatic artificial muscles, together with the analytical formulation that maps the reference knee trajectory to the corresponding actuator displacement and contraction-rate demands.

2.3.1 Actuator selection and mechanism configuration

PAMs were selected as the actuation method for their light weight, inherent compliance and biomimetic contraction behaviour [6]. The chosen actuator was the Festo DMSP-20 fluidic muscle — a McKibben-type PAM of 20 mm inner diameter and 500 mm nominal length, capable of up to 1500 N contractile force at 600 kPa and a maximum contraction ratio of approximately 25% [6], [16]. Two identical units were used to coordinate bidirectional knee flexion–extension across the gait cycle.

Each PAM was mounted along the thigh segment rather than directly across the knee, between a proximal anchor on the exoskeleton thigh frame and a distal anchor on a four-bar input link in Figure 3. This placement keeps mechanical bulk away from the knee and provides a moment arm for transmitting contraction force to the linkage. The distance between the attachment points remains within the 40–50 cm range set by the linkage geometry in Section 2.3.5, so that the actuator operates within the working stroke of the selected muscle.

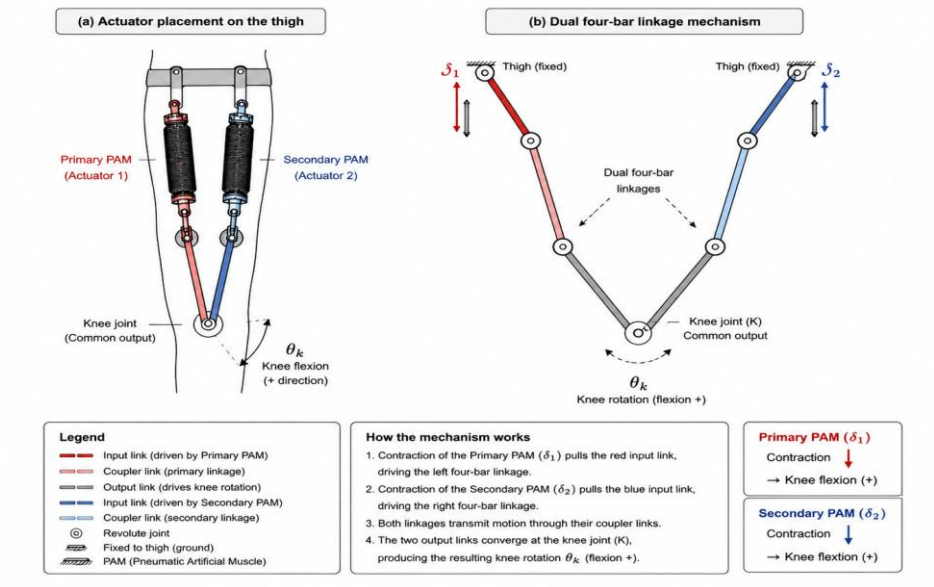


Fig. 3. Schematic of the thigh-mounted PAM-driven knee mechanism: two pneumatic artificial muscles, mounted along the thigh, independently actuate the primary and secondary four-bar linkages, which converge at the knee

Because PAMs produce linear contraction rather than rotational torque, a transmission mechanism is required. Cable-driven systems are lightweight but prone to slack and backlash, and gear-based transmissions are accurate but bulky and introduce joint backlash; linkage mechanisms are compact, backlash-free and preserve the inherent compliance of pneumatic actuation [4], [9]. A dual four-bar configuration was therefore adopted, consistent with the polycentric knee concept of Kittisares et al. [10]: each PAM independently drives one planar four-bar linkage — the primary and secondary mechanisms — whose combined action produces the resulting knee rotation. As this study addresses kinematic modelling, the actuator was selected on geometric compatibility, contraction range and compliance; detailed pressure–force modelling is reserved for future work.

2.3.2 CAD reconstruction and MotionGen simulation

The dual four-bar mechanism was modelled in CATIA V5-6R2021 (Dassault Systèmes, Vélizy-Villacoublay, France), taking the structural concept of the KNEXO exoskeleton reported by Beyl et al. [5] as the initial geometric reference. The geometry was refined iteratively to reproduce the Perry & Burnfield normative knee trajectory across the eight gait-phase boundaries; the Section 2.2 human-model trajectory serves as an independent kinematic validation of that normative reference in Section 3.1 rather than as the direct design target. The finalised model was imported into MotionGen [12] (web-based planar four-bar synthesis tool, Stony Brook University) for planar kinematic simulation. The reconstructed CAD model is shown in Figure 4.

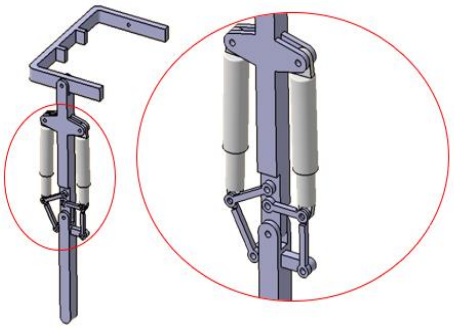


Fig. 4. Reconstructed CAD model of the dual four-bar PAM-driven knee exoskeleton, developed from the KNEXO structural concept [5]

The finalised link dimensions are listed in Table 2. The joint labels are retained throughout the manuscript to keep the CAD model in Figure 4, the MotionGen simulation in Figure 5 and the analytical derivations consistent, and the hip joint serves as the global coordinate origin, as in Section 2.2.

Table 2. Link dimensions of the primary and secondary four-bar mechanisms

Mechanism	Link	Joint	Length (mm)
Primary	Ground	GD	211.1
Primary	Input	GF	207.4
Primary	Coupler	EF	155.6
Primary	Output	DE	92.6
Secondary	Ground	DB	126.0
Secondary	Input	AB	174.0
Secondary	Coupler	CA	144.4
Secondary	Output	DC	96.3

Source: Authors' own data based on the KNEXO structural concept reported by Beyl et al. [5]

The reconstructed geometry was checked with Grashof's criterion [17]: the primary mechanism satisfied the Grashof inequality, while the secondary mechanism laid close to a change-point configuration, longest and shortest links summing to 270.3 mm against 270.4 mm for the remaining two – a difference of only 0.1 mm. Both linkages nevertheless operated as constrained rocker-rocker mechanisms, because the prescribed PAM contraction imposed a monotonic input motion that prevented either linkage from reaching a dead-centre position. Because the primary linkage satisfied the Grashof inequality and operated well away from any change-point, only the secondary mechanism required explicit transmission-angle verification. Across the eight gait events, its transmission angle remained between 80° (initial swing) and 138° (terminal swing), above the lower limit commonly taken as 40°-45° for efficient force transmission in four-bar mechanisms [17]. The 80° minimum had a wide margin from the $\theta_2 = 0$ fold associated with the near-change-point geometry, confirming that the prescribed gait input never drove the mechanism toward a dead-centre configuration. A 2 s gait-cycle input was applied in MotionGen with the hip fixed and the ankle kinematically coupled to the knee, preserving a single primary degree of freedom; the simulation reproduced all eight gait phases with continuous, non-singular linkage motion.

Because the secondary mechanism laid only 0.1 mm from the change-point condition — of the same order as typical machining tolerances (±0.1–0.5 mm) — its sensitivity to dimensional deviation was examined. The change-point produced a fold-type dead-centre at input angle $\theta_2 = 0°$; the prescribed monotonic PAM input, however, confined the secondary linkage to a transmission-angle range of 80°–138° across the eight gait events, keeping it clear of this configuration. A ±0.5 mm deviation applied to any combination of the link lengths shifted the Freudenstein constants K_1–K_3 by at most 1.2%, so the resulting contraction and contraction-rate profiles were correspondingly insensitive to dimensional deviations of this order. Fabrication should nonetheless preserve the nominal link-length ratios to maintain the transmission-angle margin.

2.3.3 Vector loop-closure and Freudenstein formulation

Because the PAMs generate linear contraction rather than independent joint torques, the mechanism cannot be treated as a serial open chain. A closed-loop vector formulation was therefore used to relate PAM contraction to knee rotation through the dual four-bar linkage [10]. The joint locations, link vectors and angle conventions are defined in Figure 5.

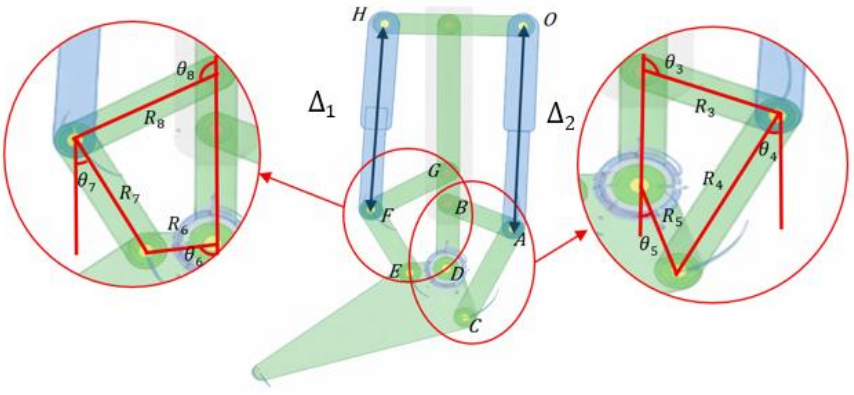


Fig. 5. MotionGen model of the dual four-bar mechanism showing the joint locations, link vectors and four-bar angles adopted as the geometric reference for the analytical derivations

Each link is represented as a planar position vector defined by its length and absolute orientation angle:

$$l_i = l_i \cos\theta_i \hat{x} + l_i \sin\theta_i \hat{y} \quad – \quad (4)$$

Differentiating with respect to time gives the link-end velocity in terms of the link angular velocity:

$$\dot{l}_i = l_i \dot{\theta}_i(-\sin\theta_i \hat{x} + \cos\theta_i \hat{y}) \quad – \quad (5)$$

which is applied in the velocity analysis of Section 2.3.6. For each four-bar mechanism, the input, coupler, output and ground links form a closed loop, so the link vectors sum to zero:

$$l_a + l_b - l_c - l_d = 0 \quad – \quad (6)$$

Expanding Eq. (6) into scalar components and eliminating the coupler angle yields the Freudenstein equation for a planar four-bar mechanism [17]:

$$K_1 \cos\theta_4 - K_2 \cos\theta_2 + K_3 = \cos(\theta_2 - \theta_4) \quad - \quad (7)$$

where θ_2 is the actuator-driven input angle, θ_4 the resulting knee rotation, and K_1, K_2 and K_3 are dimensionless constants fixed entirely by the link lengths in Table 3. For a prescribed input motion, Eq. (7) is solved numerically for the output rotation.

Table 3. Freudenstein constants for the primary and secondary mechanisms, computed from the link dimensions in Table 2; a, b, c and d denote the input, coupler, output and ground link lengths respectively

Constant	Definition	Primary	Secondary
K_1	d/a	1.018	0.724
K_2	d/c	2.280	1.308
K_3	$\frac{a^2 - b^2 + c^2 + d^2}{2ac}$	1.873	1.032

Source: Calculated by the authors from the link dimensions in Table 2

The formulation was applied independently to the primary and secondary mechanisms, with the input, coupler, output and ground links assigned per Table 2 and Figure 5. The numerically solved input–output angle pairs were verified against the Freudenstein constraint across all eight gait phases in Section 3.2, confirming consistency between the reconstructed geometry and the analytical model. These input–output relationships form the basis for the actuator stroke and velocity analyses of Sections 2.3.4–2.3.7.

2.3.4 Joint trajectory planning

A continuous multi-segment Linear Segment with Parabolic Blends (LSPB) trajectory generated a smooth knee profile across the 2 s gait cycle. The formulation produced a trapezoidal velocity profile with bounded, piecewise-constant acceleration while maintaining continuity of position and velocity at every gait-phase transition [18]. This continuity is important for PAM-driven systems, whose compliant, nonlinear contraction behaviour can amplify abrupt motion changes [6]. Unlike a single-segment LSPB, which forces the knee to rest at every waypoint, the continuous multi-segment formulation permits non-zero via-point velocities at the intermediate gait events, producing more physiologically realistic motion.

Table 4. LSPB trajectory parameters for the seven knee-joint gait segments — initial and final knee angle, segment duration, and cruise velocity

Segment	Initial angle (°)	Final angle (°)	Duration (s)	Cruise velocity (rad/s)
HS – LR	8	18	0.20	+1.3090
LR – MS	18	7	0.40	−0.6327
MS – TS	7	2	0.40	−0.2400
TS – PS	2	40	0.20	+4.3919
PS – ISW	40	60	0.26	+1.4315
ISW – MSW	60	28	0.28	−2.5077
MSW – TSW	28	0	0.26	−2.3351

Source: Calculated by the authors based on the prescribed knee trajectory and trajectory-planning method described in [18], [19]

The gait cycle was partitioned into seven trajectory segments connecting the eight gait-event boundaries of Section 2.1. The knee-angle key points were taken from the validated MotionGen simulation. Following Siciliano et al. [19], the via-point velocity at each intermediate event was assigned from the adjacent segment slopes — their mean when the slopes share a sign, and zero at a flexion–extension reversal — while zero velocity was imposed at heel strike and terminal swing. The HS and TSW knee-angle key points (8° and 0°, respectively) were not enforced to be identical: both laid within the Perry normative variability band at their respective events (HS: 0–15°, TSW: 0–8°), and the trajectory was treated as a single-stride rehabilitation profile rather than an exactly periodic limit cycle, consistent with the slow, rehabilitation-paced walking adopted here [13], [14]. Each segment used the equal-thirds blend convention, with a blend time of one-third of the segment duration [18], from which the segment cruise velocity follows. The resulting key points, durations and cruise velocities are listed in Table 4.

The highest cruise velocity in Table 4, 4.39 rad/s (≈252°/s), occurred in the terminal-stance to pre-swing segment and corresponded to the rapid pre-swing knee flexion that preceded toe-off. In normal gait, the knee flexion velocity was the greatest near toe-off [13], with normative sagittal knee angular-velocity data placing this peak on the order of 300–350°/s at natural cadence [15]; the prescribed value therefore remained below the natural-cadence peak, while exceeding a strict proportional scaling of that velocity to the slower 2 s cycle (≈3 rad/s), reflecting the brisk pre-swing flexion required to preserve toe clearance.

The seven segment velocity profiles were concatenated into a continuous knee angular-velocity profile over the gait cycle. This profile is the prescribed knee motion for the velocity kinematic analysis in Section 2.3.6 and the continuous stroke-map evaluation in Section 2.3.7.

2.3.5 Actuator stroke at gait events

Using the knee-angle key points of Table 4 with the reconstructed linkage geometry and the Freudenstein formulation of Section 2.3.3, the pneumatic actuator lengths and contractions were determined at the eight gait-event boundaries. Each PAM behaves as a prismatic actuator, so its instantaneous length is the Euclidean distance between its proximal attachment point, fixed on the thigh frame, and its distal attachment point, carried by the four-bar input link:

$$L_i = \left\| p_{d,i} - p_{p,i} \right\| \quad \text{(cm)} \tag{8}$$

The actuator contraction relative to the nominal rest length L_0 is

$$\Delta_i = L_0 - L_i \quad \text{(cm)} \tag{9}$$

where i denotes the primary or secondary mechanism and a positive Δ is a contraction from the nominal length. Eq. (8) and (9) were evaluated at all eight gait-event boundaries; the resulting lengths and contractions are listed in Table 5.

Table 5. Pneumatic actuator length L and contraction Δ at the eight gait-event boundaries (nominal rest length 50 cm; positive Δ denotes contraction)

Event	t (s)	Knee angle (°)	Primary L (cm)	Primary Δ (cm)	Secondary L (cm)	Secondary Δ (cm)
HS	0.00	8	48.89	1.11	41.48	8.52
LR	0.20	18	48.14	1.86	43.35	6.65
MS	0.60	7	49.64	0.36	41.10	8.90
TS	1.00	2	50.00	0.00	40.74	9.26
PS	1.20	40	46.63	3.37	48.23	1.77
ISW	1.46	60	42.92	7.08	50.00	0.00
MSW	1.74	28	47.08	2.92	44.76	5.24
TSW	2.00	0	50.00	0.00	40.28	9.72

Source: Calculated by the authors from the actuator kinematic equations

All actuator contractions remained within the practical range of McKibben-type muscles, below approximately 10 cm — under 20% of the nominal actuator length. The primary actuator returned to its rest length (Δ = 0) at terminal stance, and the secondary actuator reached its rest length at the initial-swing boundary (ISW), confirming that the nominal length is consistent with the extreme linkage configurations. The two actuators exhibited complementary contraction behaviour, reflecting the coordinated bidirectional action of the dual four-bar linkage. These discrete values are the reference data for the analytical stroke map of Section 2.3.7.

2.3.6 Velocity kinematic analysis

In the dual four-bar mechanism the links are joined at common revolute joints, so their angular velocities are kinematically coupled. To obtain the PAM contraction rates from the prescribed knee angular velocity, the loop-closure relation of Section 2.3.3 was differentiated with respect to time [11]. Differentiating the loop-closure condition, Eq. (6), gives the velocity loop-closure relation of Eq. (10), where the ground-link derivative is omitted because the ground link is stationary.

$$\dot{\boldsymbol{l}}_a + \dot{\boldsymbol{l}}_b - \dot{\boldsymbol{l}}_c = 0 \quad - \quad (10)$$

with each link-end velocity given by Eq. (5). Resolving this relation into scalar components yields a linear system from which the coupler- and input-link angular velocities are obtained in terms of the prescribed output (knee) angular velocity; the explicit component expressions are standard and are omitted here for brevity.

Because each PAM acts as a prismatic actuator, its rate of contraction equals the relative velocity of its two attachment points projected onto the actuator axis:

$$\dot{\Delta}_i = -\left(v_{d,i} - v_{p,i}\right).\hat{u}_i \quad \text{(cm/s)} \quad (11)$$

where û is the unit vector directed along the actuator and the attachment-point velocities are obtained from the link angular velocities through Eq. (5). Evaluating this relation for both actuators gives the contraction-rate relations that, with the stroke map of Section 2.3.7, yield the continuous actuator-rate profiles assessed in Section 3.

2.3.7 Analytical stroke map

The actuator contractions obtained at the eight gait-event boundaries in Section 2.3.5 provide a set of input–output pairs relating the knee angle θ to each actuator contraction Δ. Rather than resolving the full inverse geometry at every time step, a continuous analytical stroke map approximates the contraction directly as a function of knee angle. For each actuator, a quartic polynomial is fitted to the discrete (θ, Δ) data by least-squares regression:

$$\Delta_i(\theta) = c_{i,0} + c_{i,1}\theta + c_{i,2}\theta^2 + c_{i,3}\theta^3 + c_{i,4}\theta^4 \qquad \text{(cm)} \qquad (12)$$

A quartic is the lowest-order polynomial that captures the nonlinear curvature of the contraction profile, particularly during rapid swing-phase flexion; lower orders fitted poorly, while higher orders risk oscillatory behaviour between data points without improving accuracy [20]. The fitted coefficients are listed in Table 6, and the stroke maps reproduce the discrete data with root-mean-square errors of 0.23 cm (primary) and 0.37 cm (secondary), about 3% of the respective working stroke ranges.

Table 6. Quartic stroke-map coefficients (Eq. (12)) for the primary and secondary actuators, obtained by least-squares fitting of the gait-event data

Coefficient	Primary	Secondary
c_0	−0.2184	+9.521
c_1	+0.1281	−0.1083
c_2	-1.202×10^{-3}	-4.418×10^{-3}
c_3	$+1.088\times10^{-5}$	$+9.142\times10^{-5}$
c_4	$+1.485\times10^{-7}$	-5.384×10^{-7}

Source: Calculated by the authors using least-squares quartic polynomial fitting

Applying the stroke map to the continuous LSPB knee trajectory of Section 2.3.4 yields the continuous actuator-contraction profile, and the corresponding contraction rate follows by chain-rule differentiation:

$$\dot{\Delta}_i = \frac{d\Delta_i}{d\theta}\dot{\theta} \qquad \text{(cm/s)} \qquad (13)$$

where $\dot{\theta}$ is the prescribed knee angular velocity. The stroke map thus provides continuous actuator displacement and contraction-rate profiles without repeated inverse-kinematic computation — the computational core of the proposed framework. These profiles are evaluated in Section 3.

3. RESULTS AND VALIDATION

This section presents the kinematic results and validation of the proposed exoskeleton. The forward-kinematic gait model was first validated against normative benchmarks in Section 3.1; the reconstructed mechanism was then verified through MotionGen simulation and Freudenstein loop-closure analysis in Section 3.2; the actuator stroke behaviour was evaluated against pneumatic-muscle operating limits in Section 3.3; and the velocity kinematic response was analysed for the LSPB-driven trajectory in Section 3.4.

3.1 Validation of the human gait model

To confirm that the forward-kinematic model of Section 2.2 produces physiologically representative motion, the simulated gait characteristics were compared with established normative benchmarks. The simulated joint-angle trajectories, ranges of motion, vertical toe clearance and sagittal toe trajectory are shown in Figure 6.

The joint-angle trajectories reproduced the coordinated inter-joint motion of normal walking, with the knee reaching a swing-phase peak of approximately 57°. The simulated hip, knee and ankle ranges of motion — 40°, 55° and 25° — were compared with normative values in Table 7.

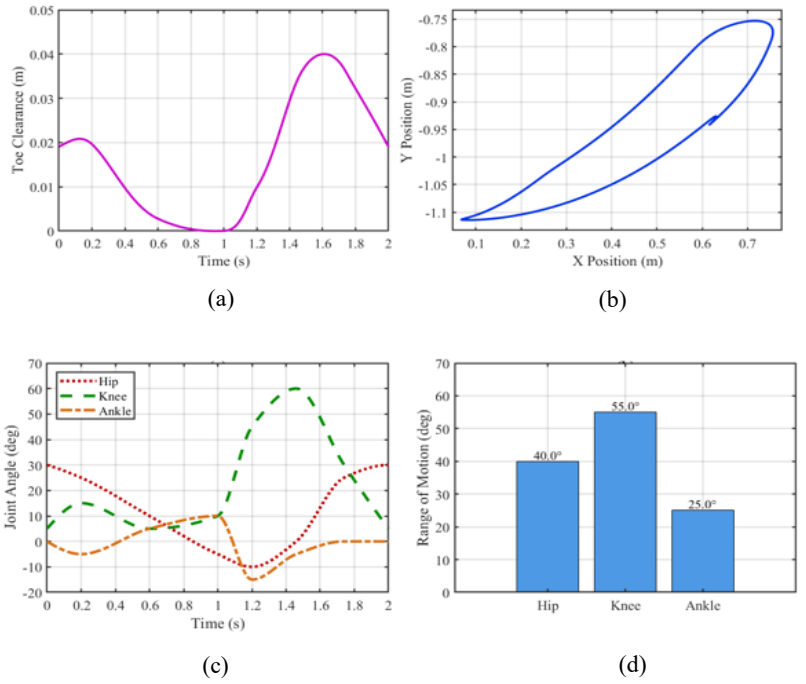


Fig. 6. Simulated lower-limb gait characteristics from the forward-kinematic model: (a) vertical toe-clearance profile; (b) sagittal-plane toe trajectory; (c) hip, knee and ankle joint-angle trajectories; (d) simulated joint ranges of motion

Table 7. Comparison of the simulated joint ranges of motion with normative literature values

Parameter	Present Study	Perry & Burnfield (2010)	Winter (2009)	Agreement
Hip ROM (°)	40.0	40 – 45	39 – 40	Within both ranges
Knee ROM (°)	55.0	55 – 65	57 – 63	At Perry lower bound; just below Winter
Ankle ROM (°)	25.0	25 – 30	25 – 31	Within both ranges
Peak knee flexion (°)	57	60 – 65	57 – 63	At Winter lower bound; below Perry
Gait cycle duration (s)	2.0	–	1.0 – 1.2	Slow, rehabilitation-paced walking

Source: Present study; normative values adapted from Perry and Burnfield [13] and Winter [15]

The vertical toe clearance reached a swing-phase peak of approximately 40 mm, sufficient for safe limb advancement. The knee values lying at the lower bound of the normal-speed ranges were consistent with the slow, rehabilitation-paced walking speed adopted here. The simulated gait characteristics agreed with normative benchmarks and provided a physiologically representative reference for the exoskeleton design of Section 2.3.

3.2 Mechanism verification and Freudenstein loop–closure

The reconstructed dual four-bar mechanism was verified through sagittal-plane MotionGen simulation and analytical Freudenstein loop-closure analysis. Figure 7 compares the reconstructed knee flexion–extension trajectory with the Perry & Burnfield normative profile.

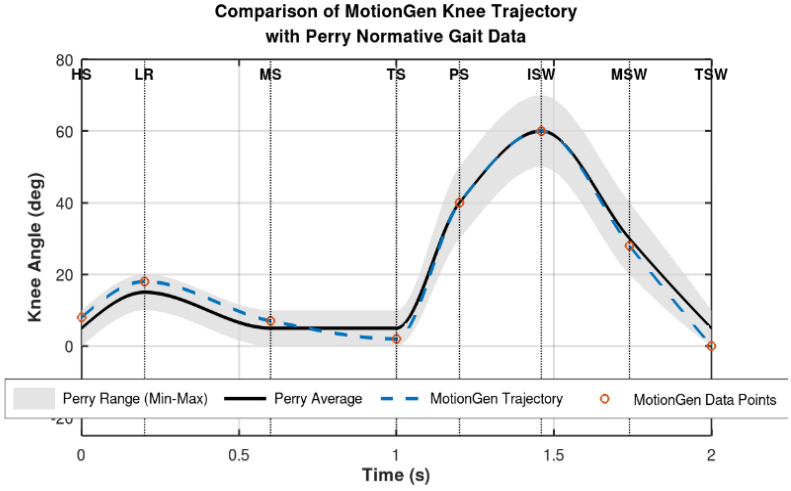


Fig. 7. Reconstructed knee flexion–extension trajectory compared with the Perry & Burnfield normative mean and variability band; the markers denote the eight gait-event boundaries

Across the gait cycle the mechanism remained extended through stance for limb support and generated progressively increasing knee flexion through swing for toe clearance, returning toward extension at terminal swing. The MotionGen-generated knee angles at the eight gait-event boundaries were compared with the Perry normative data in Table 8.

Table 8. MotionGen-generated knee angles at the gait-event boundaries against the Perry & Burnfield normative range; deviation is measured from the normative mean

Gait Event	t (s)	MotionGen knee angle (°)	Perry normative range (°)	Deviation from mean (°)
HS	0.00	8	0 – 15	+3
LR	0.20	18	8 – 22	+3
MS	0.60	7	2 – 15	–1
TS	1.00	2	0 – 8	–1
PS	1.20	40	25 – 45	+5
ISW	1.46	60	50 – 70	0
MSW	1.74	28	20 – 40	–2
TSW	2.00	0	0 – 8	–3

Source: Present study; normative values adapted from Perry and Burnfield [13]

Every MotionGen-generated knee angle fell within the Perry normative variability band. The root-mean-square error between the MotionGen trajectory and the normative mean, evaluated over the eight gait-event boundaries, was 2.69° — about 4.5% of the working knee-angle range — with a maximum deviation of 5° at pre-swing. This level of agreement is comparable to that reported for other four-bar knee exoskeleton designs [10].

The input–output angle pairs were further verified against the Freudenstein loop-closure relation, Eq. (7), at every gait-event boundary. The loop-closure residuals — the percentage difference between the two sides of the Freudenstein equation — are listed in Table 9.

Table 9. Freudenstein loop-closure residuals for the primary and secondary mechanisms at each gait-event boundary

Gait Event	Primary Error (%)	Secondary Error (%)
HS	4.09	1.14
LR	0.99	0.37
MS	2.83	4.98
TS	1.48	0.27
PS	2.42	3.17
ISW	1.95	2.94
MSW	4.90	1.79
TSW	2.01	0.75

Source: Calculated by the authors from MotionGen simulation and Freudenstein loop-closure analysis

All loop-closure residuals remained below 5%, with mean errors of 2.58% (primary) and 1.93% (secondary) and an overall mean of 2.25%. These residuals were incidental rather than systematic: the percentage difference between the two sides of the Freudenstein equation reflected the small numerical difference between MotionGen's simulated input–output angles and the analytical Freudenstein solution — both obtained for the same reconstructed linkage — rather than any inconsistency in the kinematic formulation, and they showed no monotonic trend across the gait cycle. Importantly, the near-change-point geometry of the secondary mechanism did not systematically inflate its residuals — the secondary mean (1.93%) was lower than the primary mean (2.58%), and the largest secondary residual (4.98% at mid-stance) occurred well away from any singular configuration; the secondary's transmission-angle extremes, at initial swing (80°) and terminal swing (138°), carry residuals of only 2.94% and 0.75% respectively, so residual magnitude showed no correspondence with proximity to a change-point. The isolated peaks therefore reflected local sensitivity of the output angle to the small geometric mismatch at particular configurations rather than a systematic error in the model. The magnitude observed confirms acceptable consistency between the reconstructed geometry and the analytical formulation, supporting its use in the actuator stroke and velocity analyses that follow.

3.3 Actuator stroke evaluation

The actuator stroke behaviour was evaluated using the geometric formulation of Section 2.3.5. The continuous PAM contraction profiles over one gait cycle are shown in Figure 8, and the gait-event values are those of Table 5.

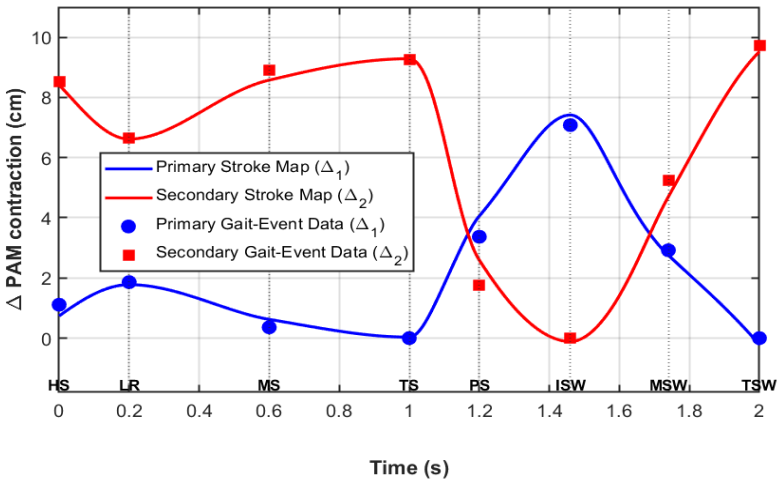


Fig. 8. Continuous PAM contraction profiles of the primary and secondary actuators over one gait cycle, computed from the quartic stroke maps; the discrete gait-event values of Table 5 are shown as markers

The two actuators exhibited complementary bidirectional contraction. During stance, the primary actuator maintained small contractions of 0–2 cm while the secondary actuator sustained larger contractions of about 6.5–9.3 cm, corresponding to the extended knee configuration that supported the limb. As the cycle entered swing, the behaviour reversed: the primary actuator contracted to a maximum of 7.08 cm near peak knee flexion while the secondary actuator extended toward its rest length, both returning toward their stance configurations through terminal swing. This complementary action is consistent with the antagonistic actuation principle of PAM-driven rehabilitation systems [5].

All contractions remained well within the practical range of the selected muscle in Table 10. The largest contraction — 9.72 cm for the secondary actuator — corresponded to a contraction ratio of 19.4% of the 50 cm nominal length, comfortably below the 25% practical limit of McKibben-type fluidic muscles. Operating below 20% is advantageous, as PAMs exhibited increasingly nonlinear force–contraction behaviour and reduced controllability at higher contraction ratios [21].

Table 10. PAM contraction range for both actuators against the practical operating limit of the selected muscle

Parameter	Primary	Secondary	PAM limit
Minimum contraction (cm)	0.00	0.00	–
Maximum contraction (cm)	7.08	9.72	12.5
Maximum contraction ratio (%)	14.2	19.4	25

Source: Present study; PAM practical operating limit based on Festo DMSP specifications [16]

The quartic stroke maps of Section 2.3.7 reproduced the discrete gait-event data with root-mean-square errors of 0.23 cm and 0.37 cm for the primary and secondary actuators — about 3% of their working stroke ranges — confirming that the analytical maps capture the knee-angle-to-contraction relationship accurately enough for the continuous trajectory evaluation.

3.4 Velocity kinematic analysis

The actuator-rate behaviour was evaluated using the vector-loop velocity formulation of Section 2.3.6, with the multi-segment LSPB knee trajectory of Section 2.3.4 as the prescribed input motion. Figure 9 shows the resulting primary and secondary PAM contraction-rate profiles over one complete gait cycle.

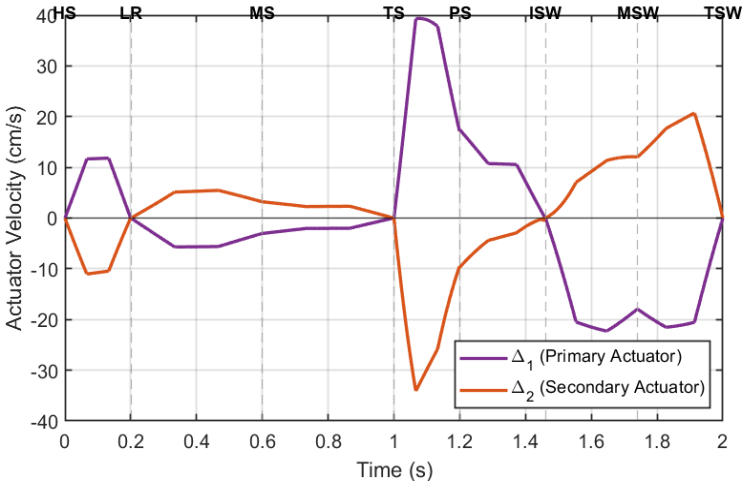


Fig. 9. Velocity kinematic analysis: primary and secondary PAM contraction-rate profiles over one complete gait cycle, obtained from the vector-loop velocity formulation

Through stance, both actuator rates remained small, within roughly ±12 cm/s. The largest transitions occurred in the terminal-stance to pre-swing region: the primary actuator reached a peak contraction rate of about 39 cm/s while the secondary actuator simultaneously extended at up to about 34 cm/s, the two acting in the complementary antagonistic manner of the dual four-bar transmission [5], [10]. The trapezoidal LSPB velocity profile produced bounded, piecewise-linear actuator-rate transitions, desirable for the smooth motion sought in repetitive rehabilitation training [6], [18].

Because the contraction rate was proportional to the prescribed knee angular velocity in Eq. (13), the actuator-rate demand scaled linearly with the trajectory. Reducing the pre-swing, knee-velocity peak from 4.39 rad/s to 3.0 rad/s – the value obtained by scaling the normative toe-off velocity to the 2 s cycle in Section 2.3.4 – lowered the peak contraction rates from 39 and 34 cm/s to about 27 and 23 cm/s for the primary and secondary actuators respectively, with a 32% reduction. The rates remained smooth, bounded and below one actuator length per second (≤0.8 L0 s-1 for the 50 cm muscle), indicating that the reduced pre-swing velocity substantially lowers the kinematically predicted actuator-rate demand.

4. CONCLUSION

This study developed an analytical kinematic framework for a PAM-driven dual four-bar knee exoskeleton that predicts actuator displacement and contraction-rate demands at the preliminary design stage. The KNEXO-derived mechanism reproduced the normative knee trajectory with a root-mean-square error of 2.69° over the eight gait-event boundaries, every gait-event angle inside the Perry normative variability band and Freudenstein loop-closure residuals below 5% for both mechanisms. All PAM contractions remained below 20% of the nominal actuator length, within the 25% practical limit of the Festo DMSP-20 fluidic muscle. The analytical quartic stroke-map reproduced the nonlinear knee-angle-to-contraction relationship with root-mean-square errors of 0.23 cm and 0.37 cm for the primary and secondary actuators, enabling continuous actuator evaluation without repeated inverse-kinematic computation.

However, several factors may introduce discrepancies between the simulated results and real-world performance, including PAM nonlinear dynamics such as pressure-dependent hysteresis, creep and time-delay behaviour, manufacturing tolerances and joint clearances in the physical linkage, soft-tissue deformation at the human–exoskeleton interface, and inter-subject variability in gait patterns. The framework is limited to sagittal-plane kinematic analysis. A trajectory-planner comparison, a dynamic actuator model, force-feasibility analysis under load, and experimental validation are reserved for future work and treated in an extended journal version of this study.

5. ACKNOWLEDGEMENTS/FUNDING

The authors did not receive any financial support from any organization for the research, authorship, or publication of this article. The authors would like to acknowledge the support and facilities provided by the affiliated institution that enabled the completion of this research.

6. CONFLICT OF INTEREST STATEMENT

The authors declare that they have no known competing financial interests or personal relationships that could have appeared to influence the work reported in this paper.

7. AUTHORS' CONTRIBUTIONS

Fariesha Jani: Conceptualization, Methodology, Investigation, Formal Analysis, Writing – Original Draft

Tuan Muhammad Ariff Ihsan Tuan Asmadi.: MotionGen Simulation, Validation, Writing – Review & Editing.

Wan Sulaiman Wan Mohamad.: Methodology, Validation, Writing – Review & Editing.

Mohd Hanif Mohd Ramli.: Supervision, Validation, Writing – Review & Editing

8. DECLARATION OF GENERATIVE AI IN THE WRITING PROCESS

During the preparation of this work, the author(s) did not use any AI-assisted technologies

9. DATA AVAILABILITY/SUPPLEMENTARY MATERIALS

The datasets used and/or analysed during the current study are available from the corresponding author on reasonable request.

10. ETHICS STATEMENT

The authors declare that this research did not involve human or animal subjects. All experimental procedures were performed following the institutional Safety, Health, and Environmental (HSE) protocols of Universiti Teknologi MARA.

11. REFERENCES

[1] V. L. Feigin, M. Brainin, B. Norrving, S. O. Martins, J. Pandian, P. Lindsay, M. F. Grupper, and I. Rautalin, "World Stroke Organization: Global Stroke Fact Sheet 2025," *Int. J. Stroke*, vol. 20, no. 2, pp. 132–144, Feb. 2025, doi: 10.1177/17474930241308142.

[2] S. J. Olney and C. Richards, "Hemiparetic gait following stroke. Part I: Characteristics," *Gait Posture*, vol. 4, no. 2, pp. 136–148, 1996, doi: 10.1016/0966-6362(96)01063-6.

[3] J. Mehrholz, S. Thomas, J. Kugler, M. Pohl, and B. Elsner, "Electromechanical-assisted training for walking after stroke," *Cochrane Database Syst. Rev.*, vol. 2020, no. 10, Art. no. CD006185, Oct. 2020, doi: 10.1002/14651858.CD006185.pub5.

[4] N. Aliman, R. Ramli, and M. S. Amiri, "Actuators and transmission mechanisms in rehabilitation lower limb exoskeletons: A review," *Biomed. Tech. (Berl.)*, vol. 69, no. 4, pp. 327–345, Aug. 2024, doi: 10.1515/bmt-2022-0262.

[5] P. Beyl, M. Van Damme, R. Van Ham, B. Vanderborght, and D. Lefeber, "Design and control of a lower limb exoskeleton for robot-assisted gait training," *Appl. Bionics Biomech.*, vol. 6, no. 2, pp. 229–243, Jul. 2009, doi: 10.1080/11762320902784393.

[6] B. Kalita, A. Leonessa, and S. K. Dwivedy, "A Review on the Development of Pneumatic Artificial Muscle Actuators: Force Model and Application," *Actuators*, vol. 11, no. 10, Art. no. 288, Oct. 2022, doi: 10.3390/act11100288.

[7] P. Beyl, M. Van Damme, R. Van Ham, B. Vanderborght, and D. Lefeber, "Pleated pneumatic artificial muscle-based actuator system as a torque source for compliant lower limb exoskeletons," *IEEE/ASME Trans. Mechatron.*, vol. 19, no. 3, pp. 1046–1056, Jun. 2014, doi: 10.1109/TMECH.2013.2268942.

[8] L. Wu, C. Wang, J. Liu, B. Zou, S. Chakrabarty, T. Bao, and S. Q. Xie, "Novel Design on Knee Exoskeleton with Compliant Actuator for Post-Stroke Rehabilitation," *Sensors*, vol. 25, no. 1, Art. no. 153, Jan. 2025, doi: 10.3390/s25010153.

[9] A. Niyetkaliyev, A. Turganbayev, M. Karasheva, R. Zhylkaidarov, and Y. Turlybek, "Exploring the Potential of Four-Bar Linkages in Robotic Exoskeletons: A Comprehensive Review," *J. Mech. Des.*,

vol. 147, no. 10, Art. no. 100801, Oct. 2025, doi: 10.1115/1.4068107.

[10] S. Kittisares, T. Ide, H. Nabae, and K. Suzumori, "Ergonomic dual four-bar linkage knee exoskeleton for stair ascent assistance," *Front. Robot. AI*, vol. 10, Art. no. 1285520, Dec. 2023, doi: 10.3389/frobt.2023.1285520.

[11] M. Gao, Z. Wang, S. Li, J. Li, Z. Pang, S. Liu, and Z. Duan, "Design and optimization of exoskeleton structure of lower limb knee joint based on cross four-bar linkage," *AIP Advances*, vol. 11, no. 6, Art. no. 065124, Jun. 2021, doi: 10.1063/5.0053899.

[12] A. Purwar, S. Deshpande, and Q. J. Ge, "MotionGen: Interactive design and editing of planar four-bar motions for generating pose and geometric constraints," *J. Mech. Robot.*, vol. 9, no. 2, Art. no. 024504, Apr. 2017, doi: 10.1115/1.4035899.

[13] J. Perry and J. M. Burnfield, *Gait Analysis: Normal and Pathological Function*, 2nd ed. Thorofare, NJ, USA: SLACK, 2010.

[14] A. Rodríguez-Fernández, J. Lobo-Prat, and J. M. Font-Llagunes, "Systematic review on wearable lower-limb exoskeletons for gait training in neuromuscular impairments," *J. NeuroEng. Rehabil.*, vol. 18, no. 1, Art. no. 22, Feb. 2021, doi: 10.1186/s12984-021-00815-5.

[15] D. A. Winter, *Biomechanics and Motor Control of Human Movement*, 4th ed. Hoboken, NJ, USA: John Wiley & Sons, 2009.

[16] Festo AG & Co. KG, "Fluidic Muscle DMSP," Product datasheet, Esslingen, Germany. [Online]. Available: https://www.festo.com/us/en/p/fluidic-muscle-id_DMSP/ (accessed May 21, 2026).

[17] R. L. Norton, *Design of Machinery: An Introduction to the Synthesis and Analysis of Mechanisms and Machines*, 5th ed. New York, NY, USA: McGraw-Hill, 2012.

[18] L. Biagiotti and C. Melchiorri, *Trajectory Planning for Automatic Machines and Robots*, 1st ed. Berlin, Germany: Springer, 2008.

[19] B. Siciliano, L. Sciavicco, L. Villani, and G. Oriolo, *Robotics: Modelling, Planning and Control*, 1st ed. London, U.K.: Springer, 2009.

[20] R. L. Burden and J. D. Faires, *Numerical Analysis*, 9th ed. Boston, MA, USA: Brooks/Cole, Cengage Learning, 2010.

[21] S. Krishna, T. Nagarajan, and A. M. A. Rani, "Review of Current Development of Pneumatic Artificial Muscle," *J. Appl. Sci.*, vol. 11, no. 10, pp. 1749–1755, 2011, doi: 10.3923/jas.2011.1749.1755.



© 2026 by the authors. Submitted for possible open access publication under the terms and conditions of the Creative Commons Attribution (CC BY-NC-ND) license (http://creativecommons.org/licenses/by/4.0/).